Broadband Photothermal Spectroscopy with a Mid-Infrared Quantum Cascade Laser Frequency Comb

BAICHUAN HUANG[1,†], GRZEGORZ GOMÓŁKA[1,2,†], TOMMI MIKKONEN[1,3,4,†], GERARD WYSOCKI[1,*]

[1]Department of Electrical and Computer Engineering, Princeton University, Princeton, New Jersey 08544, USA
[2]Department of Optics and Photonics, Wrocław University of Science and Technology, Wybrzeże Stanisława Wyspiańskiego 27, 50-370, Wrocław, Poland
[3]Photonics Laboratory, Physics Unit, Tampere University, P.O. Box 692, FI-33014 Tampere, Finland
[4]Department of Chemistry, University of Helsinki, P.O. Box 55, FI-00014 Helsinki, Finland
** Corresponding author: gwysocki@princeton.edu*
[†] These authors contributed equally to this work.

Abstract: We demonstrate a broadband photothermal spectroscopy in the mid-infrared region using a quantum cascade laser frequency comb operating between ~7.7 and ~8.2 μm covering a frequency range of ~70 cm^{-1}. The photothermal spectroscopy technique employs a Mach-Zehnder interferometer operating in a pump-probe configuration, where the mid-infrared pump beam is modulated by a Fourier transform spectrometer. A 76-m Herriott-type multipass cell is used for signal enhancement. As proof-of-concept, we have measured the photothermal spectra of nitrous oxide that shows good agreement with the HITRAN database. A minimum detection limit of 83 ppb of nitrous oxide in nitrogen is estimated from a broadband photothermal spectrum with 9.9 GHz spectral point spacing and acquired over 78 minutes. This detection scheme also provides over three orders of magnitude of photothermal signal linearity with gas concentration. This spectroscopic method combines the functionality of high sensitivity and background-free detection of photothermal spectroscopy as well as broadband mid-infrared operation of quantum cascade laser frequency comb, which could find applications in trace gas sensing systems that benefit from these features.

1. Introduction

Optical frequency combs (OFCs) are coherent light sources that increasingly find applications in diverse fields including spectroscopy, communications, and metrology as they offer wide spectral coverage, narrow linewidths, and direct optical-to-radiofrequency conversion [1,2]. The coverage provided by OFCs in the mid-infrared (mid-IR) region is particularly useful for gas sensing as this spectral range contains strong ro-vibrational bands of numerous molecules of interests [3]. Many methods have therefore been proposed to generate mid-IR comb radiation such as doping transition materials in chalcogenide hosts for femtosecond lasers [4], utilizing frequency down-conversion of near-infrared (near-IR) OFCs by difference frequency generation [5], or through optical parametric oscillation [6]. Most of these technologies, however, require a relatively large set of bulky and expensive equipment for comb generation [2,7]. The advent of quantum cascade laser frequency combs (QCL-FCs) enables direct generation of high-power coherent comb radiation with relatively broadband mid-IR coverage from semiconductor devices operated near or at room temperature [8,9]. Its self-starting comb generation only requires direct electrical pumping, which obviates sizeable equipment and can potentially enable chip-scale systems [8,10]. QCL-FCs have therefore been employed as coherent light sources in many spectroscopic applications [10–15].

One of the spectroscopic techniques which can significantly benefit from application of powerful mid-IR OFCs is photothermal spectroscopy (PTS). Similar in principle to

photoacoustic spectroscopy (PAS) where OFCs have already been used in several works [16–21], PTS is a background-free, highly sensitive spectroscopy method that utilizes the indirect effects of light absorption [22]. In PTS, light absorption causes an increase in local temperature of the sample, which induces changes in the local refractive index (RI) of the sample. The RI changes can subsequently be detected optically often using an interferometric setup operating in a pump-probe configuration, where the pump is absorbed and the probe is used for RI sensing. Several detection schemes utilizing PTS have been demonstrated, including Mach-Zehnder interferometer (MZI) [23], heterodyne MZI [24,25], dual-mode hollow-core fiber interferometer [26], and Fabry-Perot interferometer [22,27]. A great advantage of PTS is that it allows independent wavelength selection of the pump and probe lasers, so the pump can operate in the mid-IR regime to target strong ro-vibrational transitions while the probe can make use of more accessible and robust telecom-type near-IR sources, detectors, as well as optical fibers. PTS pumped in the mid-IR region was previously demonstrated with the implementation of optical parametric oscillators [28], interband cascade lasers [25], or distributed feedback (DFB) quantum cascade lasers (QCLs) [24,27], but has hitherto been limited to single-frequency pump lasers. On the other hand, broadband PTS with OFCs has been only demonstrated in the near-IR regime using an electro-optic comb as the pump source [22].

In this work, we present a proof-of-concept, broadband Frequency Comb Photothermal Spectroscopy (FC-PTS) technique using a mid-IR QCL-FC as the pump. A QCL-FC is modulated by a Fourier transform spectrometer (FTS) to induce photothermal RI modulation, which is then detected with a near-IR heterodyne interferometer. An astigmatic Herriott-type multipass cell (MPC) is employed to enhance the FC-PTS sensitivity. We demonstrate a broadband FC-PTS measurements of nitrous oxide (N_2O) with spectral point spacing of 9.9 GHz, which shows good agreement with simulations based on the HITRAN database and yields a minimum detection limit of 83 ppb. This approach combines the advantages of broadband mid-IR operation, high power, and compact footprint of QCL-FC as well as high sensitivity and background-free detection of PTS implemented with high-quality and cost-effective MZI detection leveraging telecom-type optical components. To the best of our knowledge, this is the first demonstration of broadband PTS in the mid-IR regime using a frequency comb source together with an MPC signal enhancement.

2. Operation Principle of FC-PTS

The general configuration of FC-PTS with a heterodyne MZI detection is depicted in Fig. **1**. The modes of a pump source, an OFC, are amplitude-modulated at different modulation frequencies $f_{m,i}$ prior to being directed to a gas cell containing the target gas to create photothermal effect. The i^{th} comb line in the optical frequency domain can be expressed as $v_i = v_0 + iv_r$, where i is an integer, v_0 is the carrier-envelope offset frequency, and v_r is the comb repetition frequency.

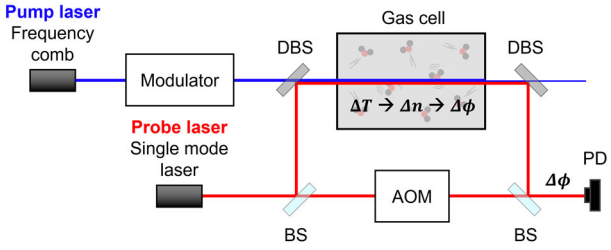

Fig. 1. The simplified scheme of FC-PTS with a heterodyne MZI detection. DBS – dichroic beamsplitter; BS – beamsplitter; AOM – acousto-optic modulator; PD – photodetector.

The temperature change ΔT_i induced from the absorption by the i^{th} comb line creates an RI change that can be expressed as [29]:

$$\Delta n_i = \frac{(n-1)\,\alpha\, P_{QCL,i}}{4\pi\, T_0\, \rho\, C_p\, r^2\, f_{m,i}} \tag{1}$$

where n is the initial RI of the target gas, α is the wavelength-dependent absorption coefficient of the target gas, $P_{QCL,i}$ is the power of the i^{th} comb line, T_0 is the temperature, ρ and C_p are respectively the density and isobaric specific heat of the target gas, r is the beam radius of the pump source, and $f_{m,i}$ is the modulation frequency of the i^{th} comb line. Assuming a uniform distribution of the RI change along the optical path, the phase shift $\Delta\phi_i$ (sensed by a probe laser colinear with the pump laser), which is related to the RI change Δn_i, can be expressed as:

$$\Delta\phi_i = \frac{2\pi\, L\, \Delta n_i}{\lambda_p} \tag{2}$$

where L is the length of the gas cell and λ_p is the wavelength of the probe laser. The modulation of the frequency comb therefore creates phase modulation of the probe laser, which is a collection of the phase modulations $\Delta\phi_i$ induced by all individual comb lines. The phase modulation can be sensitively detected in a heterodyne interferometer and subsequently converted to a photothermal spectrum via Fourier transform. From Eq. (1)-(2), it is also evident that the photothermal detection can take advantage of the high power offered by a QCL-FC as well as the increased interaction length provided by an MPC, which are both employed in this work.

3. Experiments

3.1 Rapid-scan FTS

A schematic of the system used to perform broadband mid-IR FC-PTS in a rapid-scan mode is shown in Fig. *2*. A QCL-FC centered at ~7.9 μm (~1260 cm^{-1}) with a bandwidth of ~450 nm (~70 cm^{-1}) and a repetition rate of 9.9 GHz is used as the pump source. The QCL-FC is modulated by a Michelson interferometer in a commercial FTS (Thermo Scientific Nicolet 8700) with a similar modulation scheme as the one presented in Ref. [16]. The FTS is operating in a rapid-scan mode with mirror velocity u such that each comb line with wavenumber ν_i is modulated with a frequency $f_{m,i} = 2u\cdot\nu_i$ [30]. The light emerging from the FTS is split on a beamsplitter (BS_1, CaF_2 window) which directs a small fraction (~3%) of the light to a mid-IR photodetector (PD, Vigo PVM-10.6) to capture the optical spectrum (OS) of QCL-FC, which is later used as reference for power normalization. The majority of light (>90%) transmitted through BS_1 is subsequently guided through an AR-coated germanium window, which serves as a dichroic beamsplitter (DBS), into a 76-m astigmatic Herriott-type MPC (Aerodyne Research AMAC-76) containing the sample gas. The near-IR heterodyne interferometer, in which the photothermal effects are detected, uses a 1548-nm DFB laser diode (LD, Lucent Laser 2000) as the probe laser. An erbium-doped fiber amplifier (EDFA) is used to amplify the laser to compensate for the power loss of probe light inside the MPC. The amplified probe light is split by a 90:10 fiber beamsplitter (marked as BS_2 in Fig. *2*), where the larger part is collimated using a gradient-index lens fiber collimator (marked as C in Fig. *2*) and coupled colinearly with the mid-IR beam into the MPC using the DBS. In the reference arm, the near-IR beam is guided through a piezoelectric tube (PZT) fiber stretcher used for interferometer stabilization, followed by an acousto-optic modulator (AOM) shifting the optical frequency of the beam by f_a =35 MHz as well as a fiber delay line (DL) compensating for the MPC optical path. Before entering free space, both the sensing and reference arms utilize polarization controllers (not shown) to optimize the efficiency of heterodyne beatnote at f_a. The

sensing and reference beams are combined in free space on a beamsplitter (BS_3) and guided to a fast, balanced photodetector (Newport, mod. 1617). The phase of the heterodyne beatnote at the AOM-shifted frequency f_a is demodulated by a lock-in amplifier (Zurich Instruments, HF2LI) and is used to generate photothermal interferogram, which, along with the interferogram of QCL-FC captured by the mid-IR PD, are sent to the FTS to produce photothermal spectrum and QCL-FC's optical spectrum, respectively. The phase demodulated signal is also sent through a low-pass filter to the proportion-integral-derivative (PID) controller unit (Stanford Research Systems, mod. SIM960), which controls the PZT fiber stretcher to compensate for slow phase drifts of the interferometer. Note that this drift is at few-Hz level and the feedback loop is optimized for much lower frequencies than the photothermal modulation frequency f_m, so the phase compensation does not affect photothermal signal retrieval.

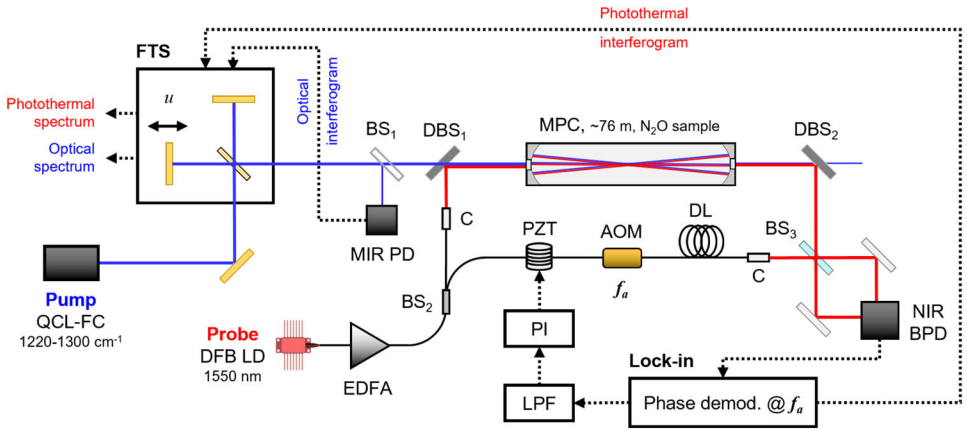

Fig. 2. A diagram of FC-PTS setup when the FTS is operating in a rapid-scan mode. MPC – multipass cell; LD – laser diode; EDFA – erbium-doped fiber amplifier; C – fiber-optic collimator; PZT – piezoelectric tube; AOM – acousto-optic modulator with frequency shift at f_a; DL – delay line; BPD – balanced photodetector. LPF – low-pass filter; PI – proportional-integral controller.

We perform spectroscopic measurements with N_2O as the sample gas for proof-of-concept demonstration. A gas mixture of 10 ppm N_2O in N_2 is filled into the MPC with pressure of 760 Torr and temperature of 21°C. The QCL-FC operating at 30.5°C with a bias current of 920 mA delivers ~70 mW of pump power into the MPC. The mirror velocity of the FTS is set to 0.079 cm/s, which modulates the pump beam at the range of frequencies centered at ~198 Hz, which is the band that provides sufficient photothermal effect and corresponds to minimal noise observed in the interferometer (the detail of which is shown in Supplementary S.1). The resolution of the FTS is set to 0.125 cm^{-1}, which corresponds to an optical path difference (OPD) of 8 cm. The phase demodulator of the lock-in that generates photothermal interferogram is set with a bandwidth of 210 Hz, which preserves the photothermal signal while attenuating high-frequency noise. The reference optical spectrum of the QCL-FC is shown in Fig. **3**(a), which spans from 1220 to 1295 cm^{-1}. Fig. **3**(b) presents the comb-line-resolved photothermal spectrum of N_2O (blue) averaged over 15 scans with a total measurement time of ~20 minutes (one interferogram is acquired every ~50 s with ~30 s of extra processing time required by the FTS). The measured photothermal spectrum of N_2O displays clear distinction from the zero-gas measurement with pure N_2 (yellow) and good agreement with the simulated photothermal spectrum (red) based on absorption spectrum from the HITRAN database and the QCL-FC OS. The large noises in the photothermal spectrum and its discrepancies from the simulation are attributed mostly to the noises in the heterodyne interferometer. This can be

addressed by longer averaging of each interferogram point in the FTS step-scan mode, which will be discussed in the following section.

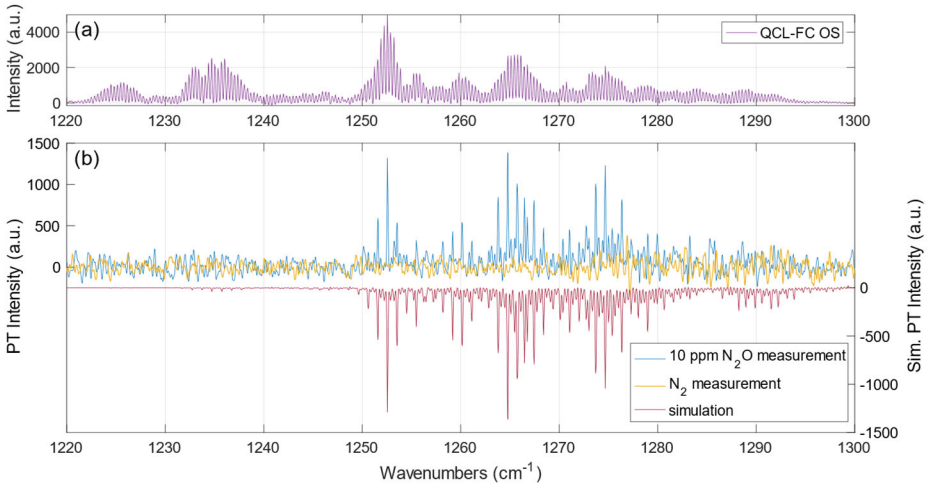

Fig. 3. Rapid-scan FC-PTS measurements of N_2O. **(a)** The optical spectrum of the QCL-FC. **(b)** Photothermal (PT) spectrum of 10 ppm N_2O (blue) and pure N_2 (yellow). The simulated photothermal spectrum based on HITRAN model and the measured QCL-FC spectrum (red) is shown for comparison and is flipped vertically for clarity.

3.2 Step-Scan FC-PTS

The performance of the photothermal spectrometer is improved when the FTS is operated in a step-scan mode, which benefits from averaging of acquired interferogram points. Instead of modulating different comb lines of the QCL-FC at different frequencies as accomplished by the rapid scan, in a step scan all comb lines are modulated at the same constant frequency $f_{m,i} = f_c$ [31], which is realized by a mechanical chopper. In the rapid-scan mode, the OFC modes are modulated at a range of frequencies, which inevitably leads to higher noise in the PTS spectrum due to the difficulty in selecting a detection band with uniformly low noise. On the contrary, the step-scan mode offers more flexibility in the choice of the modulation frequency f_c, which can be tuned to the local minimum in the noise spectrum of the interferometer. The setup of near-IR heterodyne interferometer that probes the photothermal effect is identical to the rapid-scan version, except that a second lock-in amplifier (Zurich Instruments, MFLI) performing amplitude demodulation at f_c is used to simultaneously detect and amplify photothermal and optical signals and produce corresponding interferograms. The photothermal and optical interferograms are sent to the FTS synchronously to produce photothermal and optical spectra, respectively. The step-scan FTS makes use of the single-frequency modulation and synchronous lock-in detection to attenuate the noises in the photothermal spectrum, which will be demonstrated below.

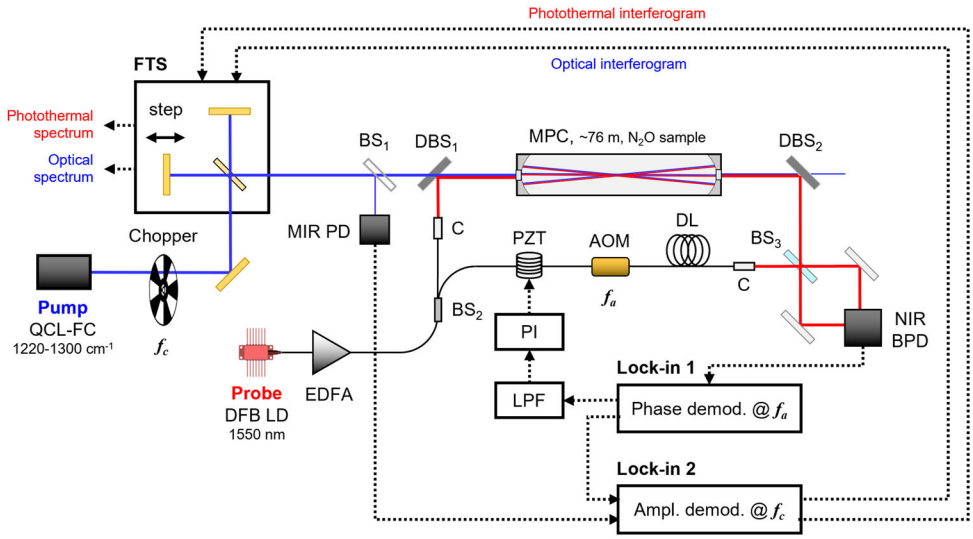

Fig. 4. The diagram of FC-PTS setup when the FTS is operating in a step-scan mode. A mechanical chopper with frequency f_c is used to modulate the pump, while a second lock-in amplifier performing amplitude demodulation (Ampl. demod.) at f_c is employed to obtain optical and photothermal interferograms.

We use the same gas mixture of 10 ppm N_2O in N_2 to demonstrate the improved sensitivity of PTS detection in the step-scan FTS mode. The mechanical chopper is set to a chopping frequency $f_c = 198$ Hz, which corresponds to minimal noise observed in the heterodyne interferometer signal (shown in Supplementary S.1). The modulation frequency f_c is set to be relatively low as the photothermal RI modulation decays with the increase of f_c (see Eq. (1)). The first lock-in demodulates the phase of the heterodyne beatnote at the AOM frequency f_a with a demodulation bandwidth of 210 Hz, which assures that the chopper-modulated photothermal signal at f_c can be conveyed without losses. The second lock-in set to f_c yields photothermal and optical interferograms by performing amplitude demodulation respectively on the photothermal signal from the first lock-in and on the signal from the mid-IR PD. In the step-scan routine, the moving mirror settles at each position for 50 ms, while the time constant of the second lock-in is set to $\tau = 15$ ms (so the mirror settling time is $> 3\tau$). This ensures steady detected signal which is then averaged for 25 ms. With 46000 mirror steps together with mirror movement and extra processing time required by the FTS, this results in the total scanning time of 78 minutes. While longer mirror settling time and longer lock-in time constant could yield higher signal-to-noise ratio (SNR), they would require longer overall scanning time. The values chosen in the experiment is the result of a trade-off between sensitivity and acquisition time.

Fig. **5**(a) and (b) depict the OPD-domain optical (of the QCL-FC source) and step-scan photothermal interferograms, respectively. A broadband comb-line-resolved photothermal spectrum is shown in Fig. **5**(d), which shows significant improvement in its signal quality provided by the step-scan FTS as compared with rapid-scan (see Fig. **5** (e)). The photothermal spectrum is later normalized by the synchronously measured comb OS presented in Fig. **5**(c) to account for the comb mode power fluctuations over the duration of the step scan. The normalized N_2O absorption spectrum is depicted in Fig. **5**(f), which shows good agreement with the simulated absorption spectrum based on the HITRAN database. The relative residual between the measurement and simulation over the entire measurement range is <10%, which is shown in Fig. **5**(g). Such measurement errors are attributed to the fluctuations of the free-running QCL-FC since it is operated without any stabilization, as well as to intrinsic noises in the heterodyne interferometer (e.g. due to any mechanical vibrations during the scan).

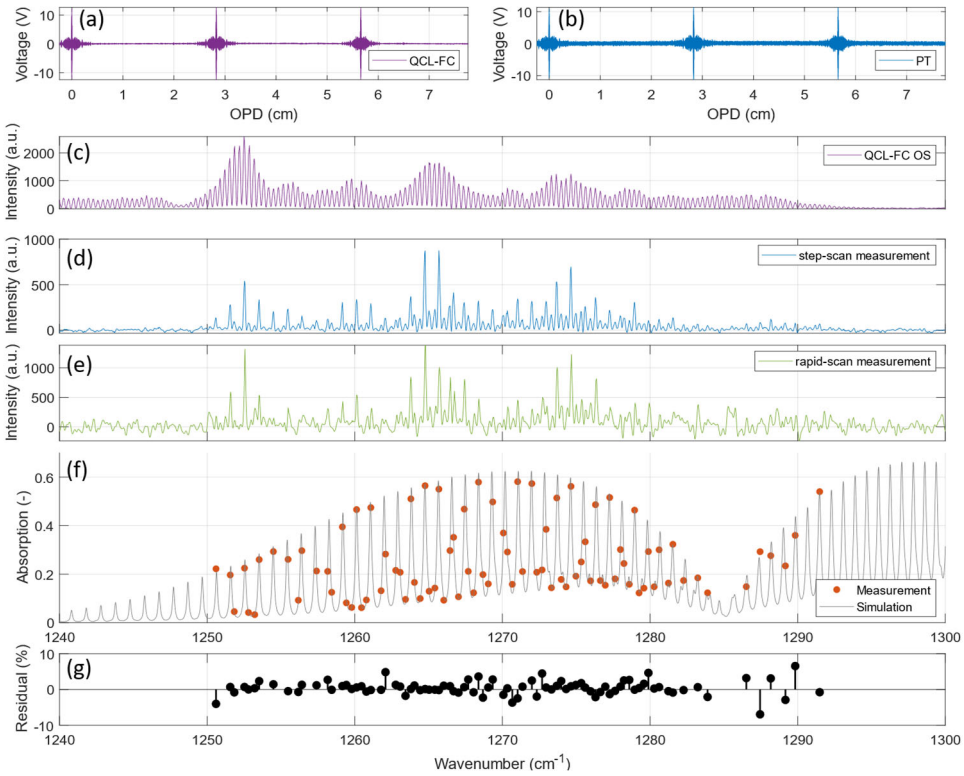

Fig. 5. Step-scan FC-PTS measurements of N_2O. **(a)** An optical interferogram acquired for QCL-FC. **(b)** A step-scan photothermal (PT) interferogram acquired for 10 ppm N_2O in N_2 mixture. **(c)** An optical spectrum calculated using (a). **(d)** A step-scan photothermal spectrum calculated using (b). **(e)** A rapid-scan photothermal spectrum discussed in Section 3.1, presented here as direct comparison. **(f)** An absorption spectrum of 10 ppm N_2O in N_2 obtained from the power-normalized photothermal spectrum (dots) plotted together with a HITRAN simulation fitted to the data. **(g)** Fit residuals.

We estimate the SNR by dividing the peak value of the photothermal spectrum (Fig. **5**(d)) at 1264.8 cm^{-1} by the standard deviation of the photothermal signal from 1210-1220 cm^{-1} where no significant N_2O absorption is observed. The presented PTS setup with the step-scan FTS achieves an SNR of 120. Therefore, a noise equivalent minimum detection limit (MDL, 1σ) of 83 ppb is estimated for this particular spectral mode of the comb, which is reached with a total QCL-FC power of 70 mW and measurement time of 78 minutes. Despite the long measurement time of the step scan, which is an important limitation of this PTS technique, this conservative single-mode MDL surpasses the reported MDL of dual-comb near-IR PTS presented in Ref. [22] and OFC-based PAS reported in Ref. [16]. This sensitivity improvement can be attributed to the advantages provided by the strong mid-IR absorption, MPC signal enhancement, and noise mitigation by the step-scan FTS. It should be noted that although the single-mode MDL is an important figure of merit for OFC-based spectrometers, if all comb modes are simultaneously considered in signal retrieval, the chemical detection limit is expected to improve as a square-root of the number of modes absorbed by the target gas with their relative contributions weighted by the amount of absorbed optical power.

3.3 Linear PTS Response

We have investigated a linearity of the response of the PTS detection scheme by monitoring the photothermal signal for a comb line targeting N_2O absorption line at 1258.79 cm^{-1} with varying N_2O concentrations. The inset of Fig. **6**(a) shows the PTS spectra used to generate PTS

signal data as a function of concentration. Note that the slight asymmetry of the spectra shown in the inset is attributed to the limited FTS resolution of 0.125 cm^{-1}, the fact that the comb mode is not precisely tuned to the center of the N_2O absorption line, and insufficient mirror settling time with respect to the lock-in time constant [32]. Overall, Fig. **6**(a) shows a good linear response of the PTS system from the MDL up to ~100 ppm where a linear fit yields $R^2 > 0.99$. Therefore, the presented step-scan PTS system achieves linearity over three orders of magnitude dynamic range of concentrations. However, the photothermal signal diverges from the linear trend beyond the 100-ppm level, and additional effects such as decrease in pump optical power within the MPC as well as other nonlinear absorption effects need to be considered.

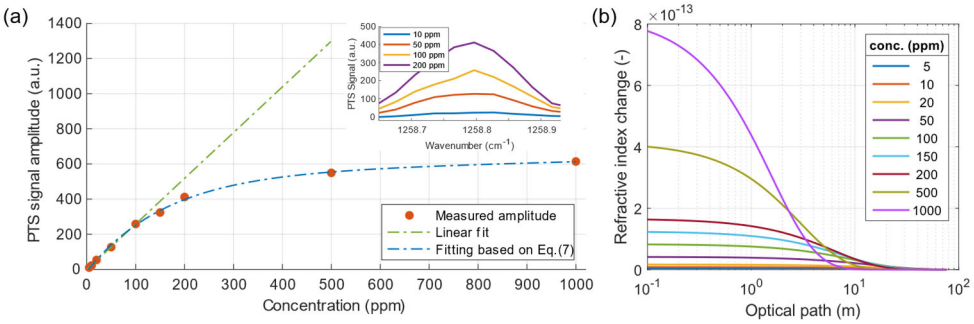

Fig. 6. (a) The response of photothermal signal amplitude at 1258.79 cm^{-1} versus N_2O concentration. A linear fitting is performed on the measured amplitudes with concentration up to 100 ppm, which exhibits good linear response (R^2 value of 0.997). Inset shows the target mode in the PTS spectrum for selected N_2O concentrations. (b) The calculated RI changes along the optical path inside the MPC for the comb line at 1258.79 cm^{-1} targeting a strong absorption line of N_2O for different concentrations, and with mirror loss coefficient calculated for MPC mirror reflectivity of 0.9881. The optical-path axis is in log scale for clarity.

We have studied the nonlinear response of the PTS system for samples with high concentrations where the amplitude of the photothermal signal clearly diverges from linear dependence (as shown in Fig. **6**(a)). In order to characterize this behavior, we need to consider the RI change Δn_i not as a uniform distribution (assumed for optically thin samples) but as a function of the optical path l.

The pump power $P_{QCL,i}$ decreases in the absorbing medium with l as:

$$P_{QCL,i}(l) = P_{QCL,i,0} \cdot e^{-\alpha l} \cdot R^N \tag{3}$$

where α is the absorption coefficient of the gas sample, $P_{QCL,i,0}$ is the initial power of the i^{th} mode of the QCL-FC, R is the reflectivity of the MPC mirrors (R = 0.9881 for our MPC) and N is the number of reflections (for a given path l it can be calculated as the floor of l/L_0, where L_0 is the MPC single-pass length of 32 cm). Since the reflectivity R is close to 1 and N is very large for the MPC, R^N can be approximated as:

$$R^N \approx R^{\frac{l}{L_0}} = e^{ln\left(R^{l/L_0}\right)} = e^{(l/L_0)\,ln\,R} = e^{-\gamma l} \tag{4}$$

where $\gamma = -\frac{ln\,R}{L_0}$.

From Eq. (1), (3), (4), the path-dependent RI change induced from the absorption by the i^{th} comb line at the path length l is:

$$\Delta n_i(l) = \frac{n-1}{4\pi T_0 \rho c_p r^2 f_m} \alpha P_{QCL,i,0}\, e^{-(\alpha+\gamma)l} \tag{5}$$

Several calculated values of $\Delta n_i(l)$ over the length of the MPC optical path for the comb line at 1258.79 cm^{-1} are shown in the Fig. **6**(b) for demonstration. One can clearly notice that the RI

change has higher initial values but decays over a shorter optical path with the increase of N_2O concentration.

In the case where the RI change distribution is highly nonuniform, the infinitesimal phase change from path length l to $(l + dl)$ is:

$$d\Delta\phi_i = \frac{2\pi\Delta n_i(l)}{\lambda_p} dl \tag{6}$$

The accumulated phase change for the total MPC length L due to absorption by the i^{th} comb line is thus achieved through integration:

$$\begin{aligned}\Delta\phi_i = \int_0^L d\Delta\phi_i &= \int_0^L \frac{2\pi\Delta n_i(l)}{\lambda_p} dl = \frac{2\pi}{\lambda_p}\frac{n-1}{4\pi T_0 \rho c_p r^2 f_m}\int_0^L \alpha P_{QCL,i,0}\, e^{-(\alpha+\gamma)l} dl \\ &= \frac{(n-1)\, P_{QCL,i,0}\, \alpha}{2T_0 \rho c_p \lambda_p r^2 f_m}\int_0^L e^{-(\alpha+\gamma)l} dl \\ &= \frac{(n-1)\, P_{QCL,i,0}\, \alpha}{2T_0 \rho c_p \lambda_p r^2 f_m}\cdot\frac{1-e^{-(\alpha+\gamma)L}}{\alpha+\gamma}\end{aligned} \tag{7}$$

The ratio $\frac{1-e^{-(\alpha+\gamma)L}}{\alpha+\gamma}$ captures the exponential decay of the optical power within the MPC, which in the limit of optically thin samples with $(\alpha + \gamma)L \ll 1$ allows for a linear approximation of the exponential factor $e^{-(\alpha+\gamma)L} = 1 - (\alpha + \gamma)L$. In this limit, the ratio term $\frac{1-e^{-(\alpha+\gamma)L}}{\alpha+\gamma}$ is simply reduced to L, which makes Eq. (7) identical with Eq. (2) used in the case of a uniform distribution of RI change. A simulation of the PTS signal for the mode at 1258.79 cm^{-1} based on a complete Eq. (7) is included in Fig. **6**(a), which captures the nonlinear dependence of the PTS signal. Thus, for optically thin samples Eq. (2) is sufficient for PTS signal modeling, but for high concentrations or stronger absorption lines, the PTS signal enters the nonlinear regime and Eq. (7) should be used for accurate signal modeling. While for moderate optical depths, Eq. (7) is sufficiently accurate in capturing the nonlinear behavior of the PTS signal, it should be also noted that for extremely optically thick samples (with unity optical depth occurring at optical paths of ~1 m) we have also observed the PTS signal decrease with concentration, which points to secondary nonlinear effects in these extreme cases that will be studied in the future.

4. Conclusions

In this work, we demonstrate the FC-PTS methodology and the characterization of system performance in a faster rapid-scan mode and in a slower, yet more sensitive, step-scan mode. The methodology shows significant potential for trace-gas sensing, and strategies to further improve the performance of the current PTS scheme are briefly discussed here.

The QCL-FC employed in this study is operated in a free-running state and is therefore susceptible to unwanted optical feedback produced by any reflective elements in the system. The main sources of optical feedback are identified to be the FTS and the MPC. Feedback attenuation by an optical isolator would effectively address this issue and stabilize laser operation, which could improve the SNR and the MDL of the system. Active stabilization of the repetition frequency of the QCL-FC by radiofrequency (RF) injection [33] can also help mitigate comb fluctuations. In addition to noise attenuation, several recently reported techniques to increase the spectral bandwidth of QCL-FCs, including dispersion management [34], RF injection [35], and optical feedback injection [36], can be integrated to enhance the detection bandwidth of the FC-PTS scheme. The spectral resolution of the PTS

scheme can be further enhanced by incorporating sub-nominal-resolution FTS technique that can achieve higher spectral resolution for targeting narrow absorption features [37]. Gapless tuning of the QCL-FC and spectra interleaving can also be utilized to measure samples with spectrally narrow absorption lines [38].

One of the challenges of the presented PTS system is the relatively long measurement time. During rapid scans, the interferogram acquisition time is determined by the FTS mirror speed (in our case 0.079 cm/s), which is directly related to the modulation frequency band and spectrometer resolution (0.125 cm^{-1} is set, which corresponds to an OPD of 8 cm). With these settings, a single interferogram is acquired every ~50 s. Faster acquisitions without loss of resolution would require faster mirror scanning that would lead to increases in the modulation frequency. Unfortunately, this would reduce the intensity of the photothermal effect (see Eq. (2) and (7)), which in free space (with relatively large cross-section beams) drops significantly at the frequencies of a few hundred Hz [39]. However, this modulation frequency threshold can be greatly increased even up to tens of kHz in hollow-core optical fiber gas cells [40]. Employment of such a gas cell could enable the use of higher mirror speed (modulation frequency), which could significantly shorten the scanning time. For our QCL-FC centered at 7.9 μm and f_m = 10 kHz, the mirror speed could be as high as ~7.9 cm/s, yielding almost 50 times shorter acquisition time. The FC-PTS scheme can also incorporate the dual-comb spectroscopy (DCS) technique, a variant of Fourier transform spectroscopy that greatly reduces measurement time [22]. This nevertheless requires full comb stabilization to create a DCS spectrum at very low frequencies suitable to perform PTS (due to inverse $f_{m,i}$ dependence, see Eq. (2) and (7)), which is significantly more difficult to achieve with mid-IR QCL-FCs as compared to near-IR, telecom-based, electro-optic modulation-based OFCs.

In conclusion, we provide the first proof-of-concept demonstration of broadband PTS in the mid-IR regime based on a QCL-FC. FTS in a rapid-scan or a step-scan mode is employed to modulate the mid-IR QCL-FC that excites the photothermal effect enhanced by the MPC, while the near-IR heterodyne interferometer is used to probe the photothermal signal. The QCL-FC allows for targeting strong, fundamental, ro-vibrational transitions of N_2O in the mid-IR regime, while the near-IR heterodyne interferometer enables detection in a convenient telecom band. The rapid-scan FTS produces a broadband photothermal spectrum of N_2O in N_2 that is in good agreement with a simulation based on the HITRAN database. On the other hand, the step-scan FTS generates an absorption spectrum of N_2O with an enhanced SNR through normalizing the photothermal spectrum to the synchronously detected comb optical spectrum, which agrees well with the simulated spectrum from HITRAN. The step-scan FC-PTS detection scheme reaches a spectral point spacing of 9.9 GHz (limited by the repetition frequency of the QCL-FC) and an MDL of 83 ppb with a pump power of 70 mW and measurement time of 78 minutes. A good linear response of PTS detection over three orders of magnitude is also realized, which shows great potential to realize applications of QCL-FCs in PTS trace gas sensing with high sensitivity and broadband spectral detection.

Funding. This work is supported in part by the Helen Shipley Hunt Fund at Princeton University, the US NSF Convergence Accelerator Program (Award #2344395), and by Thorlabs Inc. G. Gomółka acknowledges the support from Polish National Science Centre and National Agency of Academic Exchange (Preludium Bis 1, grant no. 2019/35/O/ST7/04176). T. Mikkonen acknowledges the support from the Fulbright Finland Foundation, from the Vilho, Yrjö and Kalle Väisälä Foundation of the Finnish Academy of Science and Letters, and from the Emil Aaltonen Foundation.

Acknowledgments. The authors acknowledge Kevin Lascola at Thorlabs for generously providing the QCL-FC used in this work.

Disclosures. The authors declare no conflicts of interest.

Data availability. Data underlying the results presented in this paper are not publicly available at this time but may be obtained from the authors upon reasonable request.

References

1. T. Fortier and E. Baumann, "20 years of developments in optical frequency comb technology and applications," Commun Phys **2**, 1–16 (2019).
2. L. Chang, S. Liu, and J. E. Bowers, "Integrated optical frequency comb technologies," Nat. Photon. **16**, 95–108 (2022).
3. F. Keilmann, C. Gohle, and R. Holzwarth, "Time-domain mid-infrared frequency-comb spectrometer," Opt. Lett., OL **29**, 1542–1544 (2004).
4. B. Bernhardt, E. Sorokin, P. Jacquet, R. Thon, T. Becker, I. T. Sorokina, N. Picqué, and T. W. Hänsch, "Mid-infrared dual-comb spectroscopy with 2.4 μm Cr2+:ZnSe femtosecond lasers," Appl. Phys. B **100**, 3–8 (2010).
5. A. Ruehl, A. Gambetta, I. Hartl, M. E. Fermann, K. S. E. Eikema, and M. Marangoni, "Widely-tunable mid-infrared frequency comb source based on difference frequency generation," Opt. Lett., OL **37**, 2232–2234 (2012).
6. N. Leindecker, A. Marandi, R. L. Byer, and K. L. Vodopyanov, "Broadband degenerate OPO for mid-infrared frequency comb generation," Opt. Express, OE **19**, 6296–6302 (2011).
7. M. Beiser, N. Opačak, J. Hillbrand, G. Strasser, and B. Schwarz, "Engineering the spectral bandwidth of quantum cascade laser frequency combs," Opt. Lett., OL **46**, 3416–3419 (2021).
8. A. Hugi, G. Villares, S. Blaser, H. C. Liu, and J. Faist, "Mid-infrared frequency comb based on a quantum cascade laser," Nature **492**, 229–233 (2012).
9. G. Villares, A. Hugi, S. Blaser, and J. Faist, "Dual-comb spectroscopy based on quantum-cascade-laser frequency combs," Nat Commun **5**, 5192 (2014).
10. G. Scalari, J. Faist, and N. Picqué, "On-chip mid-infrared and THz frequency combs for spectroscopy," Applied Physics Letters **114**, 150401 (2019).
11. J. Westberg, L. A. Sterczewski, and G. Wysocki, "Mid-infrared multiheterodyne spectroscopy with phase-locked quantum cascade lasers," Appl. Phys. Lett. **110**, 141108 (2017).
12. R. Santagata, D. B. A. Tran, B. Argence, O. Lopez, S. K. Tokunaga, F. Wiotte, H. Mouhamad, A. Goncharov, M. Abgrall, Y. L. Coq, H. Alvarez-Martinez, R. L. Targat, W. K. Lee, D. Xu, P.-E. Pottie, B. Darquié, and A. Amy-Klein, "High-precision methanol spectroscopy with a widely tunable SI-traceable frequency-comb-based mid-infrared QCL," Optica, OPTICA **6**, 411–423 (2019).
13. K. N. Komagata, M. Gianella, P. Jouy, F. Kapsalidis, M. Shahmohammadi, M. Beck, R. Matthey, V. J. Wittwer, A. Hugi, J. Faist, L. Emmenegger, T. Südmeyer, and S. Schilt, "Absolute frequency referencing in the long wave infrared using a quantum cascade laser frequency comb," Opt. Express, OE **30**, 12891–12901 (2022).
14. M. Lepère, O. Browet, J. Clément, B. Vispoel, P. Allmendinger, J. Hayden, F. Eigenmann, A. Hugi, and M. Mangold, "A mid-infrared dual-comb spectrometer in step-sweep mode for high-resolution molecular spectroscopy," Journal of Quantitative Spectroscopy and Radiative Transfer **287**, 108239 (2022).
15. J. Westberg, C. C. Teng, Y. Chen, J. Liu, L. Patrick, L. Shen, M. Soskind, and G. Wysocki, "Urban open-air chemical sensing using a mobile quantum cascade laser dual-comb spectrometer," APL Photonics **8**, 120803 (2023).
16. I. Sadiek, T. Mikkonen, M. Vainio, J. Toivonen, and A. Foltynowicz, "Optical frequency comb photoacoustic spectroscopy," Phys. Chem. Chem. Phys. **20**, 27849–27855 (2018).
17. J. Karhu, T. Tomberg, F. S. Vieira, G. Genoud, V. Hänninen, M. Vainio, M. Metsälä, T. Hieta, S. Bell, and L. Halonen, "Broadband photoacoustic spectroscopy of $CH_4$14 with a high-power mid-infrared optical frequency comb," Opt. Lett., OL **44**, 1142–1145 (2019).
18. T. Wildi, T. Voumard, V. Brasch, G. Yilmaz, and T. Herr, "Photo-acoustic dual-frequency comb spectroscopy," Nat Commun **11**, 4164 (2020).
19. J. T. Friedlein, E. Baumann, K. A. Briggman, G. M. Colacion, F. R. Giorgetta, A. M. Goldfain, D. I. Herman, E. V. Hoenig, J. Hwang, N. R. Newbury, E. F. Perez, C. S. Yung, I. Coddington, and K. C. Cossel, "Dual-comb photoacoustic spectroscopy," Nat Commun **11**, 3152 (2020).
20. X. Ren, M. Yan, Z. Wen, H. Ma, R. Li, K. Huang, and H. Zeng, "Dual-comb quartz-enhanced photoacoustic spectroscopy," Photoacoustics **28**, 100403 (2022).
21. Z. Wang, Q. Nie, H. Sun, Q. Wang, S. Borri, P. De Natale, and W. Ren, "Cavity-enhanced photoacoustic dual-comb spectroscopy," Light Sci Appl **13**, 11 (2024).
22. Q. Wang, Z. Wang, H. Zhang, S. Jiang, Y. Wang, W. Jin, and W. Ren, "Dual-comb photothermal spectroscopy," Nat Commun **13**, 2181 (2022).
23. W. Jin, Y. Cao, F. Yang, and H. L. Ho, "Ultra-sensitive all-fibre photothermal spectroscopy with large dynamic range," Nat Commun **6**, 6767 (2015).
24. K. Krzempek, A. Hudzikowski, A. Głuszek, G. Dudzik, K. Abramski, G. Wysocki, and M. Nikodem, "Multi-pass cell-assisted photoacoustic/photothermal spectroscopy of gases using quantum cascade laser excitation and heterodyne interferometric signal detection," Appl. Phys. B **124**, 74 (2018).

25. C. Yao, S. Gao, Y. Wang, W. Jin, and W. Ren, "Heterodyne interferometric photothermal spectroscopy for gas detection in a hollow-core fiber," Sensors and Actuators B: Chemical **346**, 130528 (2021).
26. P. Zhao, Y. Zhao, H. Bao, H. L. Ho, W. Jin, S. Fan, S. Gao, Y. Wang, and P. Wang, "Mode-phase-difference photothermal spectroscopy for gas detection with an anti-resonant hollow-core optical fiber," Nat Commun **11**, 847 (2020).
27. J. P. Waclawek, V. C. Bauer, H. Moser, and B. Lendl, "2f-wavelength modulation Fabry-Perot photothermal interferometry," Opt. Express, OE **24**, 28958–28967 (2016).
28. A. Vasiliev, A. Malik, M. Muneeb, B. Kuyken, R. Baets, and G. Roelkens, "On-Chip Mid-Infrared Photothermal Spectroscopy Using Suspended Silicon-on-Insulator Microring Resonators," ACS Sens. **1**, 1301–1307 (2016).
29. K. Krzempek, "A Review of Photothermal Detection Techniques for Gas Sensing Applications," Applied Sciences **9**, 2826 (2019).
30. J. C. Donini and K. H. Michaelian, "Effect of cell resonance on depth profiling in photoacoustic FTIR spectra," Infrared Physics **24**, 157–163 (1984).
31. L. Gonon, J. Mallegol, S. Commereuc, and V. Verney, "Step-scan FTIR and photoacoustic detection to assess depth profile of photooxidized polymer," Vibrational Spectroscopy **26**, 43–49 (2001).
32. F. Rohart, S. Mejri, P. L. T. Sow, S. K. Tokunaga, C. Chardonnet, B. Darquié, H. Dinesan, E. Fasci, A. Castrillo, L. Gianfrani, and C. Daussy, "Absorption-line-shape recovery beyond the detection-bandwidth limit: Application to the precision spectroscopic measurement of the Boltzmann constant," Phys. Rev. A **90**, 042506 (2014).
33. L. Consolino, M. Nafa, F. Cappelli, K. Garrasi, F. P. Mezzapesa, L. Li, A. G. Davies, E. H. Linfield, M. S. Vitiello, P. De Natale, and S. Bartalini, "Fully phase-stabilized quantum cascade laser frequency comb," Nat Commun **10**, 2938 (2019).
34. Q. Lu, D. Wu, S. Slivken, and M. Razeghi, "High efficiency quantum cascade laser frequency comb," Sci Rep **7**, 43806 (2017).
35. B. Schneider, F. Kapsalidis, M. Bertrand, M. Singleton, J. Hillbrand, M. Beck, and J. Faist, "Controlling Quantum Cascade Laser Optical Frequency Combs through Microwave Injection," Laser & Photonics Reviews **15**, 2100242 (2021).
36. B. Huang, N. Kosan, and G. Wysocki, "Controlled generation of harmonic states in mid-infrared quantum cascade laser frequency combs by external cavity optical feedback," Opt. Express, OE **32**, 1966–1978 (2024).
37. L. Rutkowski, P. Masłowski, A. C. Johansson, A. Khodabakhsh, and A. Foltynowicz, "Optical frequency comb Fourier transform spectroscopy with sub-nominal resolution and precision beyond the Voigt profile," Journal of Quantitative Spectroscopy and Radiative Transfer **204**, 63–73 (2018).
38. C. C. Teng, J. Westberg, and G. Wysocki, "Gapless tuning of quantum cascade laser frequency combs with external cavity optical feedback," Opt. Lett., OL **48**, 363–366 (2023).
39. U. Radeschnig, A. Bergmann, and B. Lang, "Flow-Enhanced Photothermal Spectroscopy," Sensors **22**, 7148 (2022).
40. H. Bao, Y. Hong, W. Jin, H. L. Ho, C. Wang, S. Gao, Y. Wang, and P. Wang, "Modeling and performance evaluation of in-line Fabry-Perot photothermal gas sensors with hollow-core optical fibers," Opt. Express, OE **28**, 5423–5435 (2020).